Catalysis Science & Technology

Accepted Manuscript

ROYAL SOCIETY OF CHEMISTRY

www.rsc.org/catalysis

Catalysis Science Technology

ARTICLE

Mesoporous Ni/$Ce_{1-x}Ni_xO_{2-y}$ Heterostructure as Efficient Catalyst for Converting Greenhouse Gas to H_2 and Syngas

Received 00th January 20xx,
Accepted 00th January 20xx

DOI: 10.1039/x0xx00000x

www.rsc.org/

Jie Deng,[a, b] Wei Chu, *[a] Bo Wang,[b] Wen Yang,[a] and X. S. Zhao*[b]

It has been a great challenge to develop an efficient and stable catalyst for drying reforming of methane with carbon dioxide. A new catalyst was synthesized with the catalytically active component in both the lattice and on the surface of mesoporous support. A remarkable improvement of catalytic performance of Ni nanocrystals assembled inside pore channels of mesostructured Ni-doped ceria was observed. Initial activity and long-time stability for the sample substantially surpassed those samples without the intermixed oxide and/or nonporous architecture, even though the latter were more available. Such an effect concerning collaborative function stemming from mesostructure and solid solution has been rarely reported previously in the catalysis involving CeO_2. We believe that this finding might be of much generic character and be extended to lots of similar fields. It is expected that results here can spur experimental and theoretical investigation to promote fundamental comprehension of host-guest or metal-oxide interplay in CeO_2-based composite materials

Introduction

A quite potential solution is highly necessitated to sustainably convert two abundant warming gases (CH_4 and CO_2) to value-added energy source or fuels, for mitigating the effects of global climate change. To date, some technologies were reported using carbon capture-storage-sequestration or photo-electrolysis, while forming solid carbonates by mineralization, hydrocarbons by hydrogenation, etc.[1-6] Another appealing strategy promptly gaining great concern is one-step catalytic conversion of two warming gases into versatile H_2 or syngas (which is viewed as basic building blocks or feedstock for many industrially important chemicals) applying a heat-propelled thermo-chemical process, known as CO_2 reforming of methane (CRM).[7-9] This process enables the H_2-based energy technology and fuel manufactures.

As CRM depends upon heat to propel the endothermic gas phase catalytic reaction, it is operatively much straightforward, and can achieve a higher efficiency than strategies that are built upon photo-electrolysis or traditional electrolysis. In the presence of a supported catalyst, such as metal nanoparticles (NPs) on an oxide, the CRM process proceeds via a complex mechanism involving multiple reactions, with the metal phases responsible for C–H bond cleavage, and the oxide carriers contributing to C-O bond rapture. [7, 9]

The stable C-H bonds in CH_4 (439 $kJ.mol^{-1}$), and C-O bonds in CO_2 (396 $kJ.mol^{-1}$), along with the highly endothermic nature of the CRM process require harsh operating conditions for practical reactant conversion. It is desirable to develop an efficient catalyst which is catalytically reactive at low temperatures and stable at elevated temperature.[7-8] Nickel (Ni) appears one of the most promising catalysts for CRM, though the reaction mechanism is still under debate.[7-9] Unfortunately, Ni NPs can deteriorate rapidly due to sintering of NPs and/or coking. Thus, it is extremely important to develop the stable Ni-based catalyst. The tuned positioning of the building blocks in nanoscopic level is able to strikingly enhance the behavior of catalysts via the electronic and steric interplays.[10] Materials employed for a broad spectrum of industrial, energy-related, environmental, and medical usages have made full use of the synergism between a catalyst and its carrier. Some reducible active metal oxides, e.g., ceria, are able to get involved in catalytic processes via either supplying the reactive electron/oxygen by means of producing the vacancy-related defects or altering its oxidation states along with the surface reconstructing with the metal atoms in reaction conditions.[10-13] Under such circumstance, the catalytically active centers are necessarily situated in the intimate vicinity of interphase boundaries between metallic NPs and oxide substrates.[14-15] It has been well recognized that the dual-center mechanisms wherein reagents can be catalytically activated around the metal/carrier boundaries are, really, widely present in lots of catalytic cycles.[16]

Assembling metal NPs into mesostructured materials is a peculiar example wherein the metal/carrier interplays can be notably reinforced by nanoconfinement effects.[17] The tight surrounding of metal NPs by the concave internal surfaces of physically nanosized channels can optimize the metal/carrier

---

[a] *Department of Chemical Engineering, Sichuan University, Chengdu 610065 (China).E-mail: chuwei1965@scu.edu.cn*
[b] *Department of Chemical Engineering, University of Queensland, Brisbane 4067 (Australia). E-mail: george.zhao@uq.edu.au*

† Footnotes relating to the title and/or authors should appear here.
Electronic Supplementary Information (ESI) available: [details of any supplementary information available should be included here]. See DOI: 10.1039/x0xx00000x

interfaces, resulting in state-of-the art composites for various usages. In addition to the likelihood of the enhanced activity, this metal NP-in-pore assembly provides an effective means for, to maximum extent, restricting deterioration of catalysts due to clustering of metal NPs.[18-22] Besides, stabilizing active metal phases by well-structured oxide precursors such as perovskite and solid solution gives a robust way to tune the catalytic properties of metal NPs.[23-24] Among them, the mixed-metal oxide system is compelling as promising nanocomposites in catalytic applications due to some distinct chemical properties from single metal oxides.[25-27] Inserting the second metal into the host lattice of the oxide carrier might reinforce the carrier-metal interplays and consequently influence electronic characteristics of the metal and carrier to generate superficial centers, highly reactive for breaking C–H and C-O bonds existent in reagents. In crystalline microstructural levels, the second metal can exert strain on the bulk matrix of the oxide, leading to, in such manner, generation of defective sites which might impact the immobilization of the loaded active component over oxide surfaces and change the redox functions of the whole system resulting in a better oxygen accessibility. Such effects are especially remarkable for reactions under severe conditions, as is the very case of CRM.

In this work, a new mesostructured Ni/Ni-doped CeO_2 hetero-nanocatalyst (labelled as Ni/*mp*-$Ce_{1-x}Ni_xO_{2-y}$) was synthesized and studied, with the kinetic robustness against coking and Ni-sintering, thus presenting good CRM behavior. The Ni-CeO_2 material is a kind of composite, widely applied for various reactions such as CO oxidation/methanation, CH_4 decomposition, water-gas shift reaction, hydrogenation reaction, biomass reforming, and solid oxide fuel cell,[28-32] but largely unexploited for CRM. We believe that the H_2 energy and syngas production from two greenhouse gases in the Ni-supported mesoporous Ce-Ni solid solution shown here is the example rarely reported prior, wherein reactivity and stability of Ni-catalyzed gas-phase CRM process benefits substantially from occurring within a Ni-confined $Ce_{1-x}Ni_xO_{2-y}$ mesostructure. We prepared Ni/*mp*-$Ce_{1-x}Ni_xO_{2-y}$ hetero-structures using a new and facile microwave-aided refluxed coprecipitation protocol. Our strategy was to achieve a redox-active and thermo-stable heterostructure from a cubic fluorite-typed ceria by simply doping the Ni^{2+} on the Ce^{4+} sites and introducing mesoporous frameworks.

Experimental

Catalyst Preparation

For comparison, the pristine Ni/CeO_2 sample with the same Ni loading was derived by common wet incipient impregnation using the pure CeO_2 as the support. The new Ni/$Ce_{1-x}Ni_xO_{2-y}$ samples were derived by a coprecipitation strategy employing $Ni(NO_3)_2.6H_2O$ and $Ce(NO_3)_3.6H_2O$ as precursors and NaOH (aq 0.2 M) as precipitate agent. First, each nitrate was dissolved into pure deionized H_2O separately, and then the solutions were mixed to derive a 0.1 M nitrate solution with molar ratios of Ce to Ni being 3:1 (designed as solution A); meanwhile NaOH was dissolved to the pure deionized H_2O to form a 0.2 M solution (labelled as solution B). Then, coprecipitation was conducted by mixing solutions of A and B under strong magnetic stirring, and the pH during coprecipitation was stabilized at 11. For the purpose of deriving the anticipated mesostructure, P123 was employed as the template during the coprecipitation. After finishing coprecipitation, the resulting suspension was placed in advanced microwave system to experience the 1 h aging treatment, and the microwave oven power was set to 450 W. The final slurry was subjected to washing and drying overnight at 80 °C. To stabilize the mesoporous framework, the as-prepared powders were thermally annealed at the low temperature of 200 °C for 4 h. Afterwards, the products were refluxed with ethylene diamine (EN) aqueous solution for 48 h in the temperature range of 90-100 °C, and during reflux the pH value was fixed at roughly 11.[33] Subsequently, the derived powders were filtered several times by pure deionized water, and dried overnight at 80 °C. Finally, the resultant products were initially thermally treated at 350 °C under N_2 for 4 h to stabilize the mesoporous framework and afterwards at 600 °C in air for 2 h to eliminate the organic template and enhance crystallinity. Another Ni/$Ce_{1-x}Ni_xO_{2-y}$ catalyst with no utilization of the P123 template in the precursor solution was likewise synthesized. The catalytic material with and without utilization of P123 was referred to as Ni/*mp*-$Ce_{1-x}Ni_xO_{2-y}$ and Ni/*n*-$Ce_{1-x}Ni_xO_{2-y}$.

Characterization

Chemisorption of H_2 was conducted in an auto chemisorption analyzer. The samples were first dried in helium at 250 °C for 2 h and reduced in situ by H_2 at 450 °C for 1 h at a ramp of 10 °C/min. The catalysts were flushed by helium at the reduction temperature for 2 h, and afterwards cooled down to 30 °C in vacuum to implement the chemisorption tests. H_2-temperature programmed reduction (H_2-TPR) was carried out with a fixed-bed reactor. The sample was subjected to a 4.2% H_2/N_2 mixed gas (30 mL/min) from 100 to 800 °C at a heating rate of 5 °C/min. The H_2 evolution was detected online by a SC-200 gas chromatograph with a thermal conductivity detector (TCD). X-ray diffraction patterns (XRD) were obtained with a Rigaku diffractometer using Cu K_α radiation. N_2 adsorption-desorption isotherms at -196 °C were measured on tristar II 3020. Initially, all samples were degassed at 200 °C 16 hours before tests. The specific surface areas were computed employing Brunauer-Emmett-Teller (BET) equations. Raman spectra of catalysts were recorded using an excitation wavelength of 514 nm (visible) or 325 nm (UV) on a Renishaw (RM2000) spectrometer. Element contents were obtained via inductively coupling plasma atomic emission spectrometry (ICP-AES). Thermogravimetric analysis (TGA) was performed on a Q500 thermogravimetric analyzer. The catalysts were heated in a flowing air from 25 °C to 800 °C at a ramp of 10 °C/min. Scanning electron microscopy (SEM) analysis of the samples was made using JEOL 7001, 6300 field-emission scanning electron microscope (FESEM). The UV-Vis DRS measurements were performed over the wavelength range 200-800 nm using a PERSEE TU-1901 UV-Vis NIR spectrophotometer with an integration sphere diffuse reflectance attachment. Samples were diluted in a KBr matrix by pelletization.

Reactivity Assessment

The catalytic performances were measured under atmospheric pressure utilizing a continuous fixed-bed flow reactor. Typically, the catalyst sample was diluted with the inert SiO_2 and charged into the reactor using the quartz wool. The reactant feed made up of a gaseous mixture of CH_4/CO_2 with GHSV of 12,000 mL/(h/g.cat) was adopted. The catalyst was pre-treated with H_2 at 450 ^oC for 1 h before tests. The outlet gases from the reactor were analyzed online by a GC-1690 model gas chromatograph (fitted with a TDX01 column) equipped with a thermal conductivity detector (TCD).

Results and Discussion

Structural and textural properties of as-prepared samples

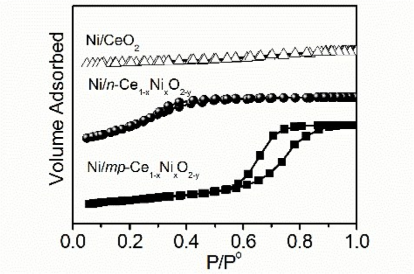

Fig.1 Isotherm of all samples.

The textural properties were examined by N_2 volumetry. As shown in Fig.1, a typical type-IV isotherm with the H1 hysteresis loop, characterized by a well-defined and steep step of N_2 uptake in a wide relative pressure (P/P^o) range of 0.55-0.90, was seen on Ni/*mp*-$Ce_{1-x}Ni_xO_{2-y}$, verifying the mesoporosity of a mesoporous channel, while this hysteretic behavior was absent for Ni/*n*-$Ce_{1-x}Ni_xO_{2-y}$ and Ni/CeO_2, revealing the nonporous nature. The initial part of the isotherm was as a result of monolayer–multilayer adsorption, and the hysteretic loop was related to capillary condensations occurring inside mesopores.[33-35] The isotherm data indicated that employing P123 as the template was robust for constructing a mesostructured skeleton in reflux phases. Because as-prepared samples were thermally annealed at as high a temperature as 600 ^oC, the results clearly indicted the formed mesostructure can withstand the demanding thermo-conditions. This is an important property for the CRM application. The good thermo-durability of this skeleton was ensured by both the inherently structural and chemical stability of the CeO_2 carrier and by the encircling EN protector that can effectively stabilize the mesoporous network against collapsing during the thermal annealing.[33] The Barrett–Joyner–Halenda (BJH) pore diameter for Ni/*mp*-$Ce_{1-x}Ni_xO_{2-y}$ was averagely 8.5 nm. In sharp contrast with other two samples, the Brunauer–Emmett–Teller (BET) specific surface area and the total pore volume for Ni/*mp*-$Ce_{1-x}Ni_xO_{2-y}$ were considerably larger (specific surface area: 20.8, 89.4, 205.1 m^2g^{-1} for Ni/CeO_2, Ni/*n*-$Ce_{1-x}Ni_xO_{2-y}$, and Ni/*mp*-$Ce_{1-x}Ni_xO_{2-y}$, respectively; total pore volume: 0.031, 0.086, 0.426 $m^3.g^{-1}$ for Ni/CeO_2, Ni/*n*-$Ce_{1-x}Ni_xO_{2-y}$, and Ni/*mp*-$Ce_{1-x}Ni_xO_{2-y}$, respectively), also unravelling a well-developed mesopore system.

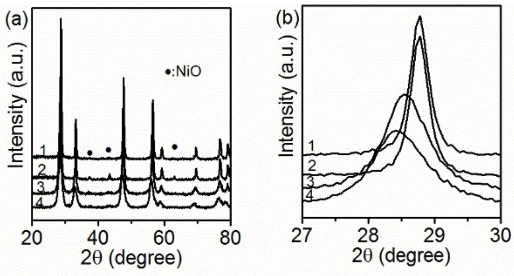

Fig.2 (a): XRD patterns of fresh CeO_2 (1), Ni/CeO_2 (2), Ni/*n*-$Ce_{1-x}Ni_xO_{2-y}$ (3) and Ni/*mp*-$Ce_{1-x}Ni_xO_{2-y}$ (4). (b): the corresponding enlargement of (111) diffraction lines shown in Fig.2 (a)

The phase structure was analysed by X-ray diffraction (Fig.2a). All samples showed the major contributions at 28.5°, 33.1°, 47.5°, 56.3°, 59.1°, 69.4°, 76.7°, and 79.1°, which can be indexed into (111), (200), (220), (311), (222), (400), (331), and (420) of the face-centred cubic (fcc) fluorite-typed structure of ceria, respectively.[36] The more broadening of these diffraction peaks for the mesostructure hinted the nanocrystalline nature of channels of mesoporous materials, meanwhile revealing that the mesostructure can effectively downsize the ceria grain. According to prior studies, this effect of stabilizing the ceria grain size can be due to the EN species that effectively protected the mesostructured ceria primary grains, and hence prolonged the improvement in the crystallization for ceria and retarded the ceria grain aggregation.[33] The peaks linked with the NiO phases were absent for both coprecipitated samples yet found for Ni/CeO_2, unveiling that Ni species were highly dispersed (< 4 nm) or incorporated into ceria lattices to form the solid solution for Ni/*mp*-$Ce_{1-x}Ni_xO_{2-y}$ and Ni/*n*-$Ce_{1-x}Ni_xO_{2-y}$ but were present on the ceria surfaces in the form of large-sized NiO crystallites for Ni/CeO_2.[37-38] By closely comparing the (111) diffraction lines for the fluorite structure (Fig.2b), it can be clearly seen that, in comparison with the pure ceria, its position shifted leftward for Ni/*mp*-$Ce_{1-x}Ni_xO_{2-y}$ and Ni/*n*-$Ce_{1-x}Ni_xO_{2-y}$ but remained nearly unchanged for Ni/CeO_2, evidencing that the Ni^{2+} ions were successfully incorporated into the ceria lattice to form a solid solution with the typical cubic fluorite structure for the binary mixed system, whereas, were practically all present as the crystalline NiO phases on the ceria surfaces for the impregnated sample.[39] Quantitative analysis by using ICP tool (samples were treated with HNO_3 before test to remove the surface Ni species as described in previously published literatures[40]) showed that the accurate contents of the Ni confined inside the ceria bulk were 13.8 %, 0.3 %, and 10.6 %, for Ni/*mp*-$Ce_{1-x}Ni_xO_{2-y}$, Ni/CeO_2, and Ni/*n*-$Ce_{1-x}Ni_xO_{2-y}$, respectively. As shown in Table S1, the Ni NP size is only 3.9 – 5.2 nm on two mixed samples and as big as 10-13 nm on Ni/CeO_2. The Ni dispersion is 7.9 % on Ni/CeO_2, 19.2 % on Ni/*n*-$Ce_{1-x}Ni_xO_{2-y}$, and 25.1 % on Ni/*mp*-$Ce_{1-x}Ni_xO_{2-y}$, while the Ni surface area is 1.82 $m^2\ g^{-1}$ on Ni/CeO_2, 2.53 $m^2\ g^{-1}$ on Ni/*n*-$Ce_{1-x}Ni_xO_{2-y}$, and 2.91 $m^2\ g^{-1}$ on Ni/*mp*-$Ce_{1-x}Ni_xO_{2-y}$. This shows that surface Ni species on two mixed samples were very dispersed and exposed. Altogether, for mixed oxides, most of Ni atoms were embedded in the ceria lattice to produce the solid solution, while the rest were highly dispersed on the solid solution surfaces to form a periodic structure of NiO.

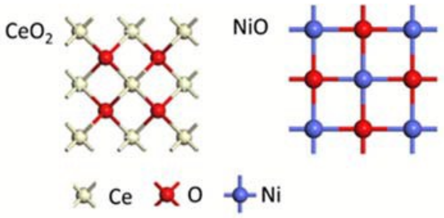

Scheme 1 Crystal structure of CeO_2 and NiO.

In fact, as illustrated in Scheme 1, the steadiest Ce or Ni oxide adopts the distinct crystalline configurations and the formal valance statuses (4+ and 2+, respectively); the coordinative number is 8 for Ce cations whereas 6 for Ni cations.[41-42] It can be predicted that, when replacing Ce cations in ceria lattice with Ni cations, the appreciable electronic and structural perturbations (such as stress, point and defects, and oxygen vacancy) in the host lattice and the extrinsic defects both near the grain boundaries and on the plane surfaces would occur, causing the shrinkage or expansion of the lattice parameter of the unit cell. In principle, when the oxidation state of alien ions is steadily 4+, we can predict the lattice parameter fluctuation by directly comparing the relative radius of two ions;[43-46] however, with the charge of alien ions unequal to that of Ce^{4+}, the lattice volume change will be governed by some other factors not only by the ion radius disparity.[47-49] In the case of the intermixed oxide of Ni in CeO_2, this situation is very complex. Some authors observed the lattice contraction after the Ni^{2+}-substitution for Ce^{4+}.[29] In contrast, in our case, a cell expansion, as reflected by the leftward shift of the ceria-assigned diffraction lines, was found. This expansion essentially arose from a combined effect by the ion radius disparity between Ni^{2+} (72 Å) and Ce^{4+} (92 Å) and the formation of the oxygen vacancy-related defects inside the ceria lattice. After the isomorphic substitution of Ni^{2+} for Ce^{4+}, the charge difference between cations induced the charge imbalance in the ceria lattice. To maintain electroneutrality, formation of oxygen vacancies and Ce^{3+} centers along with alterations in local structures emerged. The much greater ion radius of Ce^{3+} than Ce^{4+} is able to overcome, offset, or compensate the diameter disparity between Ni^{2+} and Ce^{4+}, thereby inducing the lattice expansion. To verify this inference, next, we closely analysed the structural and electronic perturbations of all samples.

Bulk and Surface Defects

Raman spectroscopy was used for elucidating bulk and surface structural defects because it is sensitive to vibrational structures of both M-O arrangement and lattice defects. The visible excitation laser line can penetrate into the deep inner layers of CeO_2 and thus reflect the bulk information of CeO_2. As shown in Fig.3a, for all samples, the predominant strong peaks centred at 460 cm^{-1} are characteristic of the first-order Raman active mode of the fluorite-type lattice (F2g), which can be viewed as an intrinsic symmetric breathing mode of oxygen atoms around cerium ions (O-Ce-O).[50-55] Compared to ceria and impregnated sample, the broadening and red shift of this mode on coprecipitated samples, particularly for Ni/*mp*-$Ce_{1-x}Ni_xO_{2-y}$, were observed. This change in F2g was attributed to the variation in the M-O vibration frequency when substitution with the dopant which account for the disparity in the ionic radius. The ionic radius disparity between cations allows the lattice parameter variations because of cell shrinkage or expansion. Hence, vibrations are rapid for shrinked lattice and slow down for expanded lattice so that the band shifted to the higher and lower wave numbers, respectively.[50-54] These reflected that symmetry of the cubic fluorite structure was notably disturbed and lowered due to the changed lattice spacing and Ce-O bond distance. Besides, on coprecipitated samples, some well-defined weak second-order Raman bands, which pertained to the lattice disorder or defects in the ceria lattice such as oxygen vacancy, phonon confinement, or inhomogeneous strain, were detected near 260 cm^{-1}, 550 cm^{-1}, 600 cm^{-1}, and 1180 cm^{-1}, further confirming the formation of $Ce_{1-x}Ni_xO_{2-y}$ solid solution with the Ni^{2+} ions replacing the Ce^{4+} ions in the CeO_2 lattice. The bands around 600 cm^{-1} represented the longitudinal optical (LO) mode of ceria, which stems from the relaxation of symmetry rules that can be associated with the intrinsic defects in the ceria lattice. This was attributed to a localized substitution defect vibration. These intrinsic defects were reportedly either the Ce^{3+}, trapped in octahedral sites, or vacancy-interstitial (Frenkel-type) oxygen defects, which were formed in the way that oxygen anions in ceria relocate themselves from tetrahedral sites to octahedral sites leaving vacancies in tetrahedral sites and localizing the excess electrons on the adjacent Ce cations.[51] The bands emerging at 550 cm^{-1} belonged to the defect-induced modes (D band), which were possibly responsible for Ce-O-Ni bonds or oxygen vacancies induced inside ceria lattices to keep electroneutrality upon replacement of Ce^{4+} with Ni^{2+}. The peaks at 260 cm^{-1} corresponded to the second-order transverse acoustic (2TA) mode of ceria while the one at 1180 cm^{-1} to the second-order longitudinal (2LO) mode of ceria.[50-55]

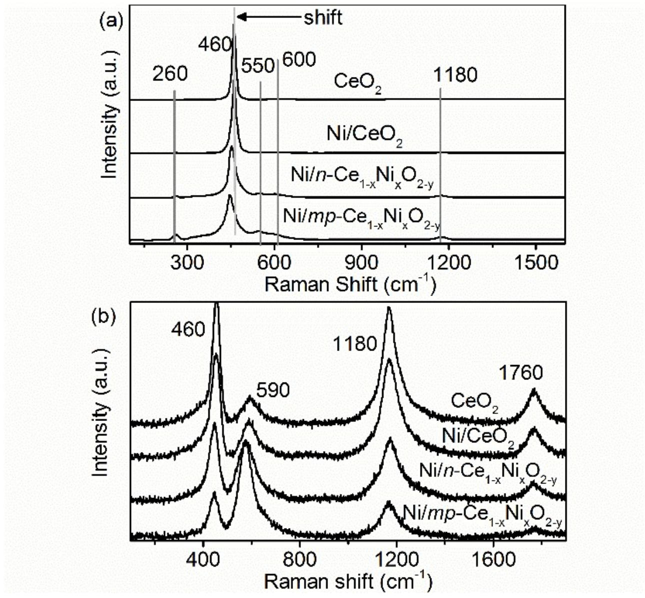

Fig.3 Visible (λ_{ex} = 514 nm) (a) and UV (λ_{ex} = 325 nm) (b) Raman spectra of all samples.

Due to the resonance Raman Effect, the samples can strongly adsorb in the UV region, and thus the UV laser line detected the outer surface information of ceria. As shown in Fig.3b, when employing the UV laser line (325 nm), the bands at 550 and 600 cm^{-1} conflated as a wide peak and the peaks near 460 cm^{-1} got substantially attenuated relative to those applying a visible laser line. The 2LO band was as intense as the F2g mode while the third overtone band (3LO) likewise arose near 1760 cm^{-1}. This marked intensification for the LO overtones in UV excitation originated from the multiphonon excitation by the resonance Raman Effect. In addition, the LO mode possessed the similar strength to the F2g mode. As for Ni/*mp*-$Ce_{1-x}Ni_xO_{2-y}$, the LO band exceeded the F2g mode in intensity, clearly there being the most surface defect sites, in line with the previous report that the inner concave surfaces of mesoporous walls can expose more defects or exert strain. So, the mesostructure showed a preference for increasing the surface defects. This may be as a result of the crystallographic surface termination by the different morphostructure or the area-volume effect by the large specific surface area and small grain size. The relative intensity ratio of the $(I_D+I_{LO})/I_{F2g}$ mirrored the defect concentration such as oxygen vacancies, and it followed the sequence: Ni/*mp*-$Ce_{1-x}Ni_xO_{2-y}$ > Ni/*n*-$Ce_{1-x}Ni_xO_{2-y}$ > Ni/CeO_2. Conversely, the NiO-indexed bands near 520 cm^{-1} were not discernable, much possibly because of a shadowing effect by the long tailing of F2g mode.

Surface oxidation state

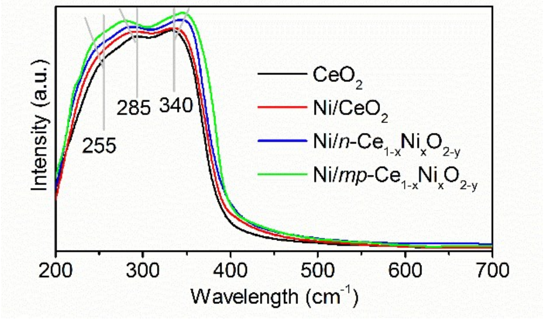

Fig.4 UV-vis diffuse reflectance spectra of all samples.

UV-vis DRS was employed to gain insights into the surface coordination and different oxidation states of samples by checking the d-d, f-d transitions and oxygen-metal ion charge-transfer bands. As shown in Fig.4, the pure CeO_2 presented three adsorption maxima near 255 nm, 285 nm, and 340 nm. The latter two well-resolved absorption maxima corresponded to the $O^{2-}\rightarrow Ce^{4+}$ charge transfer and inter-band transitions, respectively, and the poorly identified former one was ascribed to the $O^{2-} \rightarrow Ce^{3+}$ charge transfer transition.[56-58] For both intermixed oxides, in particular Ni/*mp*-$Ce_{1-x}Ni_xO_{2-y}$, the adsorption enhancement and band shift obviously occurred, suggesting the increase in the low-coordinated cerium cations. The red-shift of interband transition can arise from the existence of Ni^{2+}, which induced a pronounced rise in the Ce^{3+} concentration over surfaces, thus increasing the charge-transfer gap between the O2p and Ce4f orbitals. The blue shift of the charge transfer transitions implicated the occurrence of abundant oxygen vacancies. Hence, the UV-vis DRS confirmed that doping the Ni^{2+} at the Ce^{4+} sites of the mesostructured CeO_2 indeed facilitated the formation of the undercoordinated Ce^{3+}, increased the oxygen vacancy concentration, and induced the charge redistribution-compensation mechanism.

Redox Properties

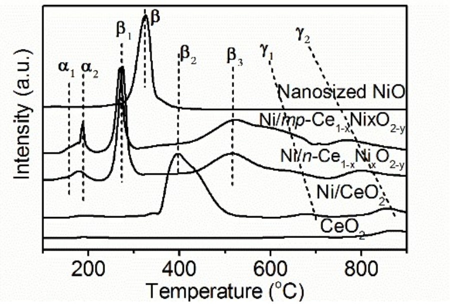

Fig.5 TPR profiles of pure CeO_2, Ni/CeO_2, Ni/*n*-$Ce_{1-x}Ni_xO_{2-y}$, Ni/*mp*-$Ce_{1-x}Ni_xO_{2-y}$, and nanosized NiO.

Taken together, it can be clearly seen from above that a Ni NP-confined mesoporous Ce-Ni solid solution with a noted structural and electronic perturbations was derived. A crucial first evaluation on feasibility of this material in the CRM usage is to identify degree of redox kinetics and ability for oxygen mobility. Shown in Fig.5 is temperature-programmed reduction by H_2 of all samples. There emerged two envelopes for the pure CeO_2, a very weak one at 655 °C (γ_1) and a big broad one ranging from 780 °C to 900 °C (γ_2), which were relevant to the reduction of the outermost and innermost shell lattice oxygen of ceria, respectively.[59] The nanosized NiO gave a single symmetric peak at 320 °C (β). For Ni/CeO_2, the peak centred at 380 °C (β_2) belonged to large aggregated NiO particles. The shift of the reduction temperature to the high temperature was caused by the large granule size (as verified by XRD data) which retarded the H_2 diffusion inside the particulate to complete its reduction.[37, 60] However, the hydrogen consumption for the mixed phase oxides was distinct from that for Ni/CeO_2, and divided into the multiple well-characterized regions. The low temperature peaks below 230 °C (α_1 and α_2) was assigned to the surface oxygen species adsorbed on the surface oxygen vacancies, caused by generation of Ce-Ni solid solutions.[61] As discussed above, the solid solution was formed by dissolution of Ni^{2+} in the CeO_2 lattice to replace Ce^{4+}, and thus the charge imbalance and lattice distortion in CeO_2 resulted in oxygen vacancies that adsorbed oxygen molecules on oxide surfaces. These adsorbed oxygen molecules were very reactive oxygen species and ready to be reduced by H_2 at low temperatures. Therefore, the intensity of the α_1 and α_2 region can be determined by population of oxygen vacancy on oxide surfaces; consistently with the structural and electronic analysis, the particular architecture of Ni/*mp*-$Ce_{1-x}Ni_xO_{2-y}$ can adsorb the affluent oxygen species over the surfaces. This is also a critical indicator for excellent oxygen mobility to enhance the carbon removal rate during CRM.

The reductive process of Ni for mixed metal oxides evolved into two different steps. The peaks near 270 °C (β_1) with a low temperature tail were responsible for the highly dispersed NiO species on the intermixed metal oxide matrix surfaces because the very small Ni particles can expose more surfaces to H_2.[62]

The peaks centred at 515 °C (β_3) were due to the complex NiO species which strongly interacted with CeO_2.[63] Integrated with the structural data, it can be indexed to the Ni species included inside the CeO_2 lattice. The considerably higher reduction temperature than the pure, aggregated, or highly dispersed NiO species clearly showed that the Ni-O bond in the solid solutions was stronger than that in the bulk NiO. This strong Ni-O bond in the solid solution arises from the fact that when occupying the Ce^{4+} sites the Ni^{2+} was forced to possess a very large number of oxygen neighbours forming the stronger $Ni\leftrightarrow O\leftrightarrow Ce$ exchange in the fluorite structure than the $Ni\leftrightarrow O\leftrightarrow Ni$ interaction in the rock salt structure. The wide bumps at 550 °C, as the shoulder peaks of β_3, represented the γ_1, hinting that the reduction of Ni inside CeO_2 was simultaneously accompanied by the reduction of surface lattice O^{2-} anions. The reduction of the bulk ceria (γ_2) shifted to as low a temperature as 720 °C, nearly 100 °C, lower than the pure CeO_2. The maxima reduction temperature of γ_1 and γ_2 on Ni/*mp*-$Ce_{1-x}Ni_xO_{2-y}$ was about 40 °C and 50 °C lower than those of Ni/*n*-$Ce_{1-x}Ni_xO_{2-y}$, respectively; their peak intensity was larger. Notably, γ_1 got merged with β_3 to a big wide peak on Ni/*mp*-$Ce_{1-x}Ni_xO_{2-y}$ but got separated from β_3 on Ni/*n*-$Ce_{1-x}Ni_xO_{2-y}$, hinting the smaller activation barrier for removing O species in fluorite structures on Ni/*mp*-$Ce_{1-x}Ni_xO_{2-y}$. Given structural data, its good redox may stem from big surface areas and more stress/defects in bulk. The large surface exposes more surface Ce ions. Due to distinct micro-chemical environment between CeO_2 surface and bulks, surface Ce ions are prone to have a low coordination number. Thus, more surface undercoordinated Ce ions were seen on Ni/*mp*-$Ce_{1-x}Ni_xO_{2-y}$. As surface O atoms are bonded by fewer nearest neighbours (smaller coordination number than the bulk), they will get readily mobile/removable. The stress and defects in the solid solution, caused the CeO_2 lattice to expand, destabilizing the fluorite structure and weakening the Ce-O bond, Thus, O^{2-} anions around Ce cations became more easily removed by H_2. In addition, the highly dispersed Ni particles were easily reducible at low temperatures, which can cause the H species activated on the Ni^o surfaces to spillover onto the fluorite structure further catalysing the reduction of CeO_2.

Indeed, H_2-TPR data implied a robust synergy between Ni and Ce species which substantially favoured the redox kinetics of the Ni/*mp*-$Ce_{1-x}Ni_xO_{2-y}$. This reduction depth directly amounted to the larger cycle capability and thus possibly more efficient generation of H_2 energy and syngas supposing that the re-oxidation of CeO_2 with CO_2 was adequately facilitated. The much lower onset temperature for removing the oxygen species of the fluorite structure unequivocally meant that the Ni/*mp*-$Ce_{1-x}Ni_xO_{2-y}$ heterostructure potentially had a smaller reduction enthalpy (or the lower oxygen diffusion/activation energy barrier) than other samples. Lately, the reduction enthalpy has been considered as a critical indicator to appraise the feasibility of the candidate catalysts for application to CRM.[7-9] On the whole, the magnitude of the reduction enthalpy or the oxygen diffusion/activation energy barrier determined the rate boundaries at which the support-mediated redox catalytic cycle could be well established. The typical redox behavior for Ni/CeO_2 put this material under the circumstance of the oxygen accessibility being much lower. In sharp contrast, it can be envisaged that the Ni/*mp*-$Ce_{1-x}Ni_xO_{2-y}$ composite trended in a better direction since the H_2 energy and syngas generation under typical CRM condition (600-800 °C) will well proceed with the Ni metal phase being active for C–H bond cleavage to form the CH_x species and H_2, and the oxide carrier providing the sufficient oxygen species by activating CO_2 to oxidize the CH_x into syngas.

Catalytic Performance Improved by Heterostructure

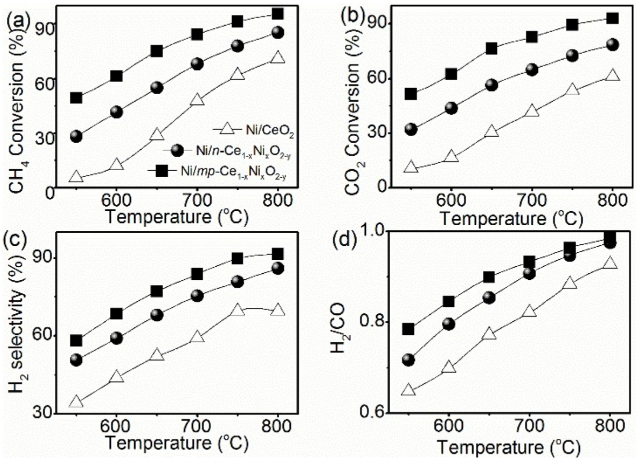

Fig.6 The effect of temperature on the CH_4 conversion (a), CO_2 conversion (b), H_2 selectivity (c), and H_2/CO ratio (d) over all samples.

The initial catalytic activity as function of temperature was shown in Fig.6. The initial catalytic reactivity was found to be strongly dependent upon the reaction temperature. Both CO_2 and CH_4 conversions for all samples significantly increased with the increment in the reaction temperatures, revealing the endothermic nature of CRM. All catalysts presented their greatest initial reactivity at 800 °C in the temperature range investigated. In addition, the CO_2 conversion was larger than that of CH_4 for all catalysts at the low temperature below 700 °C. This was caused by the concurrent occurrence of the reverse water-gas shift (RWGS) reaction ($CO_2 + H_2 = H_2O + CO$). Nonetheless, the greater CH_4 conversion than that of CO_2 was seen for all samples between 750 and 800 °C. This can be contributed to by two factors: the exothermic RWGS was oppressed when ramping up the reaction temperatures; the thermodynamically favourable CH_4 decomposition occurred violently at high reaction temperatures. Analogous behaviors for Ni-based catalysts have also been reported before.[64] Most noticeably, the much higher reactant conversions were discovered on Ni/*mp*-$Ce_{1-x}Ni_xO_{2-y}$ relative to Ni/*n*-$Ce_{1-x}Ni_xO_{2-y}$ at the same temperatures in the whole temperature ranges studied, while Ni/*n*-$Ce_{1-x}Ni_xO_{2-y}$ exhibited higher activity than the conventionally impregnated Ni/CeO_2. Such disparity can be the cooperative result of the high dispersion, good redox, and large specific surface area. The highly dispersed Ni nanoparticles were well confined or distributed in the pore channels of the redox-active and large specific surface area solid solution; therefore, more active sites were provided and the catalyst can contact and interact with reactants adequately.

The H_2 selectivity (Fig.6c) showed the similar trend to the reactant conversion, and this was owing to the fact that the elevated reaction temperature facilitated the H_2 production via different reactions, for example, water-gas shift reaction (WGS), carbon gasification, and CH_4 decomposition. These reactions more preferentially took place at elevated temperatures and could have generated H_2. The Ni/*mp*-$Ce_{1-x}Ni_xO_{2-y}$ yielded the notably larger H_2 selectivity than any other two samples. The H_2 selectivity at 700 ^oC was 83.8 %, 75.4 %, and 59.1 % for Ni/*mp*-$Ce_{1-x}Ni_xO_{2-y}$, Ni/*n*-$Ce_{1-x}Ni_xO_{2-y}$, Ni/CeO_2, respectively.

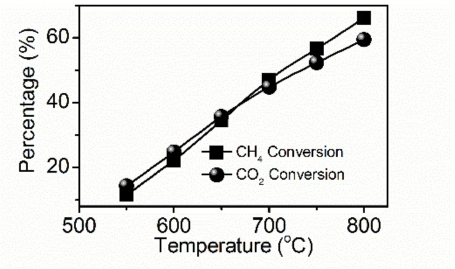

Fig.7 Initial activity on the Ni-SBA-15 catalyst.

The H_2/CO ratio (Fig.6d) was between 0.6 and 1.1 over the whole temperature range investigated and rose with the growing temperature. This value was substantially below unity particularly at the low temperatures because H_2 was consumed at low temperature by the side reactions such as RWGS, or methanation reaction. Yet, it increasingly approached the unity at the elevated temperature, due to the fact that the high temperature favoured the formation of H_2 by means of WGS, carbon oxidization, and CH_4 cracking. Among all samples, this ratio approached the CRM stoichiometric value the most at each temperature while employing the Ni/*mp*-$Ce_{1-x}Ni_xO_{2-y}$ material, manifesting that the fewest side reactions occurred over this material in the course of the reaction. The discrepancy among three catalysts in terms of initial reactivity and H_2/CO ratio signified an appreciably positive impact imparted by this particular catalyst configuration of Ni/*mp*-$Ce_{1-x}Ni_xO_{2-y}$. This promoting effect was even more encouraging considering that the diffusion of reactants and products into and out of the pore channels ought to impede the reaction to some degree in comparison with that on the freely accessible open surfaces. Apparently, the remarkably various reactivity of Ni/*mp*-$Ce_{1-x}Ni_xO_{2-y}$, Ni/*n*-$Ce_{1-x}Ni_xO_{2-y}$, and Ni/CeO_2 cannot be linked with the number of the particles since the loadings of the active Ni phase in three samples and the original diameter of the Ni particulates in both coprecipitated samples were analogous. In addition, the exclusive contribution from the geometrical impacts of the pore channels upon the catalytic functions within the mesoporous Ce-Ni solid solution was excluded using a comparison test with the mesoporous silica SBA-15 functioning as the catalyst carrier, which gave an obviously poorer reactivity than the Ni/*mp*-$Ce_{1-x}Ni_xO_{2-y}$ (Fig.7), despite that SBA-15 also had an analogous cylindrical channel with the pore diameter of 7-8 nm, and hence can impart an analogous dimensional or steric confinement for the Ni metal grains. This showed pore walls actually participated in mechanic process by boosting metal/carrier synergy. Detailed reasons for selecting Ni/SBA-15 as control test can be found in ESI.

A final appraisal of the catalyst practicability for CRM is stability. To compromise the catalytic performance and energy consumption, 700 ^oC was opted as optimal reaction temperature to assess long-term durability of materials within this study, and the results were shown in Fig.8. For Ni/*mp*-$Ce_{1-x}Ni_xO_{2-y}$, the invariable level of the converted reactants plus the formed H_2 and CO during the 2400 min test was inspiring and suggested that the performance remained stable and there was no material degeneration mechanism in action. The CH_4 conversion, nearly identical to the CO_2 conversion when they changed with time on steam, coincided with the stoichiometric coefficients for CRM. This excellent behavior must be only relevant to the particular Ni NP-confined fluorite typed Ce-Ni solid solution mesostructure. In accordance with the trend for the initial activity data in Fig.6, the Ni/*n*-$Ce_{1-x}Ni_xO_{2-y}$ gave an activity and stability, relatively inferior to Ni/*mp*-$Ce_{1-x}Ni_xO_{2-y}$ but much superior to Ni/CeO_2. The CH_4 and CO_2 conversion somewhat declined from 67.9 % and 64.7 % to 40.3 % and 52.6 %, respectively, indicating that a moderate decay occurred for Ni/*n*-$Ce_{1-x}Ni_xO_{2-y}$. Nevertheless, for Ni/CeO_2, both the CH_4 and CO_2 conversion sharply plummeted from 47.8 % and 41.6 % to 23.6 % and 23.2 % even only after 1200 min of time on stream, while the CO and H_2 selectivity as well as the H_2/CO ratio decreased significantly. For both Ni/*n*-$Ce_{1-x}Ni_xO_{2-y}$ and Ni/CeO_2, the CH_4 conversion was lower than the CO_2 conversion, implying a serious imbalance for the formation rate between the CH_x and the CO_2-derived O species during the stability test. Combined with the observations that the H_2/CO ratio was smaller than the ideal values (unity) and a small quantity of water was detected in cold trap, it can be inferred that this high CO_2 consumption was caused by the occurrence of reverse water gas shift instead of its direct dissociation activation by the defect sites on CeO_2. The production of H_2O has been shown to be able to accelerate sintering of nickel metal particles. The poor activity and unexpected product distribution for Ni/*n*-$Ce_{1-x}Ni_xO_{2-y}$ and Ni/CeO_2 revealed lack of available reactive sites for CRM. Overall, catalytic stability for all materials increased in the following sequence: Ni/CeO_2 < Ni/*n*-$Ce_{1-x}Ni_xO_{2-y}$ < Ni/*mp*-$Ce_{1-x}Ni_xO_{2-y}$.

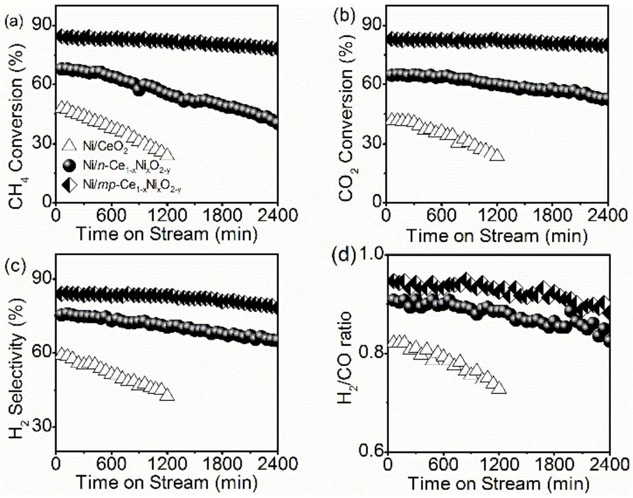

Fig.8 The results of stability test over the samples.

Characteristics of Spent Catalysts

According to previous study,[65-66] the catalytic activity decay during CO_2-CH_4 reforming was mainly due to the coking occurring over active sites. The main pathway for generating the carbon residuals can proceed as follows:

$2CO \rightarrow C + CO_2$ (Boundard reaction)

$CH_4 \rightarrow C + 2H_2$ (Cracking)

The carbon deposits formed can be eliminated by the oxidation ($O + C \rightarrow CO$ or $2C + 2OH^- \rightarrow CO + H_2O$)

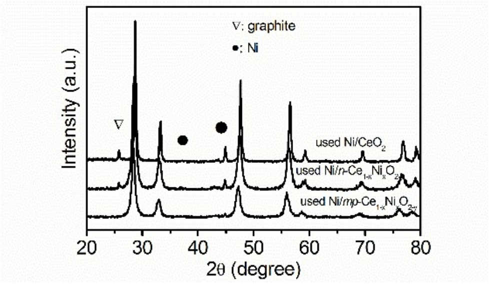

Fig.9 XRD patterns of used Ni/CeO_2 (1200 min), Ni/*n*-$Ce_{1-x}Ni_xO_{2-y}$ (2400 min), and Ni/*mp*-$Ce_{1-x}Ni_xO_{2-y}$ (2400 min).

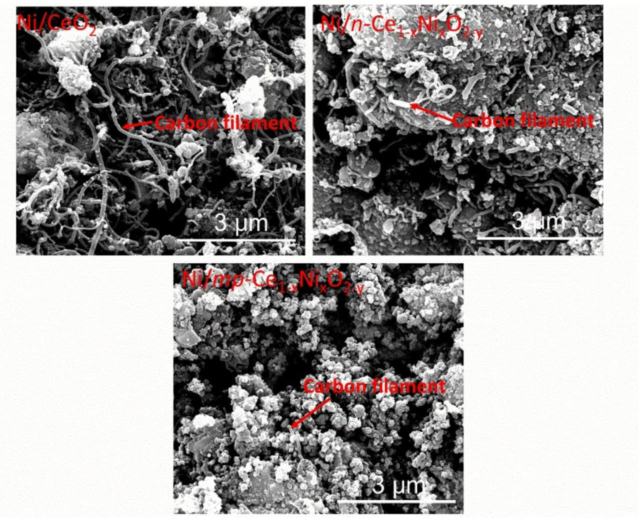

Fig.10 SEM images of used Ni/CeO_2 (1200 min), Ni/*n*-$Ce_{1-x}Ni_xO_{2-y}$ (2400 min), and Ni/*mp*-$Ce_{1-x}Ni_xO_{2-y}$ (2400 min).

The spent samples were analysed using XRD, SEM, and TG-DTA to study the reasons behind the catalytic degradation. In XRD data (Fig.9), the used Ni/*mp*-$Ce_{1-x}Ni_xO_{2-y}$ nearly presented the same pattern to the fresh one, save that the CeO_2 crystallinities grew slightly. Importantly, indistinguishability of the Ni phase-assigned diffraction peaks clearly suggested the highly dispersed small-sized Ni crystals were effectively stabilized during CRM reaction. However, for other spent samples, in particular Ni/CeO_2, strong signals for Ni species near 44° and graphitized carbons at 26° emerged, demonstrating that the severe Ni sintering and carbon deposits occurred during the reaction. Quantitatively (Table S1), the Ni NP size is still below 6 nm on Ni/*mp*-$Ce_{1-x}Ni_xO_{2-y}$ but notably grew to 13-17 nm on Ni/*n*-$Ce_{1-x}Ni_xO_{2-y}$ and 22-28 nm on Ni/CeO_2 after reaction; Ni surface area and dispersion were kept on Ni/*mp*-$Ce_{1-x}Ni_xO_{2-y}$ but fell sharply over others. In SEM micrographs (Fig.10), filamentous carbons were observed on used Ni/CeO_2 and Ni/*n*-$Ce_{1-x}Ni_xO_{2-y}$ but practically invisible for Ni/*mp*-$Ce_{1-x}Ni_xO_{2-y}$. Amounts of filamentous carbons was the most for Ni/CeO_2. Thus, graphitic peaks observed in XRD data can reasonably be ascribed to the filamentous carbon deposits.

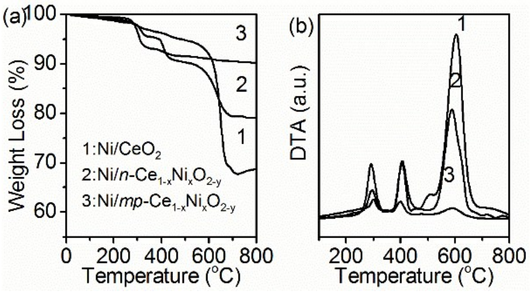

Fig.11 TG/DTA profiles of used Ni/CeO_2 (1200 min), Ni/*n*-$Ce_{1-x}Ni_xO_{2-y}$ (2400 min), and Ni/*mp*-$Ce_{1-x}Ni_xO_{2-y}$ (2400 min).

TG-DTA analysis (Fig.11) was used to quantify the overall amounts of carbon species and identify their types and thermal stability. Total weight loss derived from gasification of carbon species increased in following orders: Ni/CeO_2 > Ni/*n*-$Ce_{1-x}Ni_xO_{2-y}$ >Ni/*mp*-$Ce_{1-x}Ni_xO_{2-y}$, and their corresponding coking rates were Ni/CeO_2 > Ni/*n*-$Ce_{1-x}Ni_xO_{2-y}$ > Ni/*mp*-$Ce_{1-x}Ni_xO_{2-y}$, respectively. This showed that the scenario of coupling the mesostructure with the intermixed metal oxide played an important role in oppressing the carbon depositing. DTA curves of catalysts indicated that an exothermal process, viz., oxidation of the deposited carbon, occurred. Three exothermic peaks were detected in DTA profiles of spent samples, suggesting existence of three kinds of carbon residuals with the various reactivities formed on Ni active sites. It has been well documented that different types of carbon species can be formed on Ni-based catalytic materials due to CH_4 complete decomposition ($CH_4 \rightarrow C + 2H_2$) and Boudouard reaction ($2CO \rightarrow CO_2 + C$).[67-69] And oxidizing inactive carbons needed a much higher temperature relative to reactive carbons. Hence, exothermic peaks at the low temperatures between 170 and 300 °C represented the burning of the reactive carbon (C_α), which was active intermediate carbonaceous species for production of syngas. Peaks ranging from 300 to 420 °C were ascribed to the less-active amorphous carbons (C_β), which were formed from α-carbon by further dehydrogenation, polymerization, and rearrangement when lacking in oxidant species or at lower oxidizing rates. The exothermic peaks at high temperatures above 600 °C were linked with oxidation of inert carbons with various extents of graphitization (C_γ), which was hard to remove and can cause catalytic materials to finally deactivate. The C_γ was produced when C_β dissolved in Ni crystals, then precipitated, nucleated, and grew into the filament-shaped graphitic carbons. Obviously, the C_α was mainly detected on Ni/*mp*-$Ce_{1-x}Ni_xO_{2-y}$, while the C_β and C_γ were predominant for Ni/CeO_2 and Ni/*n*-$Ce_{1-x}Ni_xO_{2-y}$. This implied that modification of the surface configuration or structure of Ni/*mp*-$Ce_{1-x}Ni_xO_{2-y}$ effectively prevented the nucleation and growth of carbon, leading to a good equilibrium between the carbon deposition and its removal. Overall, Ni/*mp*-$Ce_{1-x}Ni_xO_{2-y}$ had a good resistance to the carbon deposition while the main reason for the fast deactivation over Ni/CeO_2 and Ni/*n*-$Ce_{1-x}Ni_xO_{2-y}$ could be explained as carbon formation from CH_4 decomposition or Boudouard reaction which could not be timely eliminated by the CO_2-derived oxygen species.

Structure-Activity Relationship

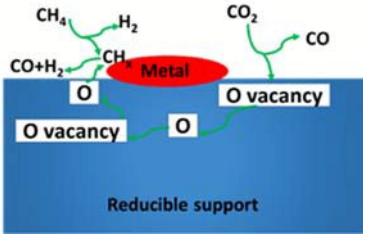

Scheme 2 Mechanic illustration of CRM over the metal/reducible supports.

In this work, one-step thermochemical conversion of notorious greenhouse gases into clean H_2 energy and versatile syngas was studied on different Ni-CeO_2 catalysts. Tuning morphostructure of nanocatalysts was found potentially advantageous to CRM. The exceptional behavior was reflected in high initial activity, excellent anti-coking/sintering, and good long-time stability. The effective engineering with these attractive advantages was fulfilled by integrating the mesoporous framework with the intermixed metal oxide to directly construct a Ni NP-confined mesoporous Ce-Ni solid solution heterostructure using simple procedures. According to prior studies[7-9], a carrier-mediated redox bifunctional mechanism for CRM using metal NPs anchored on reducible carrier materials is strongly suggested. As shown in Scheme 2, (1) CH_4 dissociates on metals to CH_x + H*, (2) H* partially reduces carrier in metal peripheries, (3) CO_2 decomposes on carrier near metal NPs to CO + O*, (4) various O species on carrier are transported onto metals to clean it from coke, and (5) O* re-oxidizes the carrier. By steps above, a dynamic equilibrium is well built to keep sustainable activity. In light of this mechanism, the good behavior of the Ni/*mp*-$Ce_{1-x}Ni_xO_{2-y}$ nanocomposite can be collaboratively dominated by following unique features.

First, the synergic effect between Ni and CeO_2, as shown by TPR, altered the electronic structure of Ce and Ni and thus modified the adsorption/desorption behavior of reactant species over them. Actually, the interplay between Ni and CeO_2 was an electronic interaction in that Ce is rich in the d-electrons and Ni possesses unfilled d-orbitals which can accept d-electrons from Ce leading to an increment in the d-electron density of the Ni atom.[70-72] Dissociation of CH_4 preferentially occurs when the empty anti-bonding orbital of C–H bond σ* of CH_4 molecules interplays with the high density of occupied Ni 3d states near Fermi levels.[73] Thus, the donating nature of enhanced Ni 3d band states reinforced the interplay between the d states and the σ*, activating the adsorbate CH_4 molecules bonded to Ni sites. Besides, as clearly unravelled by structural/electronic data above, surfaces of mesostructured fluorite typed Ce-Ni solid solutions were defect-sufficient (such as oxygen vacancies and Ce^{3+} cations), and these defect sites were positively charged. In addition to enhancing the dispersion of the reduced Ni over mixed oxide surfaces, oxophilic defect sites on Ni/*mp*-$Ce_{1-x}Ni_xO_{2-y}$ can also strongly attract negatively charged O atoms in CO_2 molecules, loosen, and cleave C-O bonds to dissociate CO_2 with concurrent formation of O species adsorbed on defective sites.[3,74] More importantly, because of the low reduction enthalpy or small oxygen activation/diffusion energy barrier, as shown by TPR, these O species on CeO_2 can be rapidly transferred or spillovered to contacted metal-support interface perimeters via Mars–van Krevelen redox cycle mechanism so that CH_x fragments from CH_4-dissociation on active metal surfaces were timely oxidized by these oxygen species into H_2 and CO prior to their massive buildup and transition to graphitic carbons, thus effectively refreshing Ni active sites. The substantial CO and syngas formation shown by activity even at very low temperatures indicated the efficient dissociative activation of reactants at active centres. Such enhanced adsorption of both CO_2 on defects sites and CH_4 on Ni sites expedited the formation rate for oxidant species and CH_x fragments, respectively, and thus promoted the H_2 and syngas production activity. The low coking rate and the good O availability clearly suggested that the O transfer rate was rapid enough to match or emulate the CH_4 dissociation rate, and thus a dynamic balance between carbon formation and its removal was well established. Contrastingly, for Ni/CeO_2 and Ni/*n*-$Ce_{1-x}Ni_xO_{2-y}$, defect-deficient CeO_2 surfaces and the low density of occupied Ni 3d states declined the affinity to oxidic CO_2 donor electrons and oxophilic CH_4 acceptor electrons, respectively.

Second, the size effect of highly dispersed Ni NPs also contributed a lot to the behavior. It has been found that the coking rate and crystalline structures of carbon deposits are highly dependent on Ni NPs sizes.[75-78] Ni NPs below a certain critical size range will have a low growth rate and small yield for filamentous carbons. This is because small sized Ni crystallinities have a large carbon saturation concentration, and, thus, induces a small driving force for atomic carbons to dissolve in Ni clusters, then precipitate, nucleate, and finally grow into filamentous carbon. Despite the close initial Ni NP size on two mixed samples, it kept stable on Ni/*mp*-$Ce_{1-x}Ni_xO_{2-y}$ but much sintered on Ni/*n*-$Ce_{1-x}Ni_xO_{2-y}$ during reaction. The increased NP size can cause some consequences: (1) lose the available Ni sites limiting CH_4-activation, (2).decrease interface areas deterring the O transfer from CeO_2 across boundaries, (3) augment the driving force for the carbon filament growth. Thus, an acute imbalance of carbon formation rate and its removal rate occurred over reaction time, yielding abundant filament cokes. Since filamentous carbons are highly crystalline and thermal stable, they cannot be removed under CRM conditions once they are formed. As evidenced, filamentous carbons can encapsulate active Ni phases, destroy catalyst structures, block catalyst beds, and eventually deactivate catalysts. And diameter of filamentous carbons is determined by size of Ni NPs, and typical diameter of filamentous carbons (15-30 nm) is much larger than size of Ni NPs of Ni/*mp*-$Ce_{1-x}Ni_xO_{2-y}$. Thus, as shown by TG, the lowest coking rate and the least crystalline and stable carbons were seen for Ni/*mp*-$Ce_{1-x}Ni_xO_{2-y}$ which had the smallest and most stable Ni NP size.

Third, the mesoporous framework provided a particular confinement effect. Via elaborately modulating the synthesis technology within our current study, comparably nanosized Ni NPs were highly distributed on nonporous and mesoporous fluorite-type Ce-Ni solid solution. Yet, Ni NPs presented the distinct anti-clustering function in CRM conditions, with highly dispersed Ni NPs well maintained for Ni/*mp*-$Ce_{1-x}Ni_xO_{2-y}$ but significantly agglomerated for Ni/*n*-$Ce_{1-x}Ni_xO_{2-y}$. Given similar preparation conditions, their distinct robustness against clustering was able to exclusively be ascribed to distinct porous systems. Large surface area mesostructure in Ni/*mp*-Ce$_{1-x}$Ni$_x$O$_{2-y}$ supplied enough inner concave channels to accommodate Ni NPs and thus led to an additional physical diffusion barrier for Ni NPs migration. Therefore, the Ni growth and sintering was greatly impeded for mesostructure. In addition, close contact of inner concave walls of mesopores with small sized Ni NPs can maximize metal/support interfaces, which can further enhance the metal-support interaction and offer more boundary areas for oxygen/electrons to transport across, thereby greatly facilitating occurrence of support-mediated redox bifunctional mechanisms. These advantages were not found in case of the unconfined Ni NPs even though Ni NPs before reaction were ultrasmall.

Conclusions

In sum, an enormous challenge to promote thermochemical catalysis of CRM is the identification of feasible catalysts. Industrial usage are built upon the low-cost and earth abundant materials that can operate in demanding reaction conditions and meanwhile maintain the high and stable performance. Here, we demonstrate that all principal aspects of CRM heterogeneous nanocatalysts, including the small size of Ni NPs, interplay between Ni and CeO$_2$, and good redox of support materials, can be concurrently boosted by simply constructing the hetero-structure of small sized Ni highly dispersed on mesoporous Ni-doped ceria. These multiple synergies resulted in exceptional catalytic behavior. Strategy here provides a desirable solution to intrinsic issues of loaded metal catalysts for CRM, such as the active phase sintering and coking. Interestingly, a notable behavior improvement can be fulfilled by introducing the randomly oriented mesoporosity and the mixed oxide. It can be expected that the subsequent amenability of the cubic fluorite-typed ceria structure to the doping/substitution, optimization of geometrical configuration, spatial orientation, and periodic regularity, physical diameter of the mesostructure, should open a tremendous engineering space, wherein even more efficient materials can be cogently explored that will expedite industrial application of economical and sustainable energy source formation predicated upon thermochemically converting warming gases and a broad controllability of catalytic properties for the customized applications can be achieved.

Acknowledgements

This work was supported by National Basic Research Program of China (973 Program, No. 2011CB201202) and the National Natural Science Foundation of China (21476145). Australian Research Council (ARC) is acknowledged for funding DP130101870. The Centre for Microscopy and Microanalysis (CMM) at The University of Queensland is acknowledged.

Notes and references

‡ Footnotes relating to the main text should appear here. These might include comments relevant to but not central to the matter under discussion, limited experimental and spectral data, and crystallographic data.

1 T. V. Choudhary, V. R. Choudhary, *Angew. Chem. Inter. Ed.* 2008, **47**, 1828-1847.
2 S. Perathoner, G.Centi, *ChemSusChe*m, 2014, **7**, 1274-1282.
3 S. C Yang, W. N.Su, J.Rick, S. D. Lin, J. Y. Liu, C. J. Pan, J. F.Lee, B. J. Hwang, *ChemSusChem,* 2013, **6**, 1326-1329;
4 R. Zhang, L. Guo, C. Chen, J. Chen. A. Chen, X. Zhao, X. Liu, Y. Xiu, Z. Hou, *Catal. Sci. Technol.*, 2015, **5**, 2959-2972.
5 P. Gao, L. Zhong, L. Zhang, H. Wang, N. Zhao, W. Wei, Y. Sun, *Catal. Sci. Technol*., doi: 10.1039/C5CY00372E
6 M. V. Landau, R. Vidruk, M. Herskowitz, *ChemSusChem*, 2014, **7**, 785-794.
7 M.S. Fan, A. Z. Abdullah, S. Bhatia, *ChemCatChem,* 2009, **1**, 192-208.
8 D. Liu, R. Lau, A. Borgna, Y. Yang, *Appl. Catal. A.: Gen.*, 2009, **358**, 110-118.
9 V. Sadykov, V. Rogov, E. Ermakova, D. Arendarsky, N. Mezentseva, G. Alikina, N. Sazonava, A. Bobin, S. Pavlova, Y. Schuurman, C. Mirodatos, *Thermochim. Acta,* 2013, **567**, 27-34.
10 Y. Y. Du, Q. Jin, J. T. Feng, N. Zhang, Y. F. He, D. Q. Li, *Catal. Sci. Technol*., 2015, **5**, 3216-3225.
11 N. J. Divins, I. Angurell, C. Escudero, V. Pérez-Dieste, J. Llorca, *Science,* 2014, **364**, 620-623.
12 G. Zou, Y. Xu, S. Wang, M. Chen, W. Shangquan, Catal. *Sci. Technol.*, 2015, **5**, 1084-1092.
13 S. Sun, D. Mao, J. Yu, Z. Yang, G. Lu, Z. Ma, *Catal. Sci. Technol.*, 2015, **5**, 3166-3181.
14 Q. Fu, H. Saltsburg, M. Flytzani-Stephanopoulos, *Science*, 2003, **301**, 935-938.
15 J. A. Rodriguez, S. Ma, P. Liu, J. Hrbek, J. Evans, M. Pérez, *Science,* 2007, **318**, 1757-1760.
16 I. X. Green, Tang, W.; Neurock, M.; Yates, Jr. J .T. *Science*, 2011, **333**, 736-739.
17 H. Liu, K. Tao, C. Xiong, S. Zhou, *Catal. Sci. Technol.*, 2015, **5**, 405-414.
18 C. M. A. Parlett, K. Wilson, A. F. Lee, *Chem. Soc. Rev.*, 2013, **42**, 3876-3893
19 N. Wang, X. Yu, K. Shen, W. Chu, W. Qian, *Inter. J. Hydrogen Energy*, 2013, **38**, 9718-9731.
20 N. Linares, A. M. Silvestre-Albero, E. Serrano, J. Silvestre-Albero, J.García-Martínez, *Chem. Soc. Rev.*, 2014, **43**, 7681-7717.
21 L. C. Chen, H. Cheng, C. W Chiang, S. D. Lin, *ChemSusChem*, 2015, **8**, 1787-1793.
22 M. Almadi, A. Nambo, J.B. Jasinski, P. Ratnasamy, M. A. Carreon, *Catal. Sci. Technol*., 2015, **5**, 380-388.
23 T. Hayakawa, H. Harihara, A. G. Andersen, A. P. E. York, K. Suzuki, H. Yasuda, D. K. Takehira, *Angew.Chem. Int. Ed.*, 1996, **35**, 192-195.
24 K. Takehira, T. Shishido, M. Kondo, R. Furukawa, E. Tanabe, K. Ito., S. Hamakawa, T. Hayakawa, *Stud. Surf. Sci. Catal*., 2000, **130**, 3525-3530.
25 S. Surnev, A. Fortunelli, F. P. Netzer, *Chem. Rev*., 2013, **113**, 4314-4372
26 D. J. Stacchiola, S. D. Senanayake, P. Liu, J. A. Rodriguez, *Chem. Rev.,* 2013, **113**, 4373-4390.
27 J. Deng, M. Cai, W. Sun, X. Liao, W. Chu, X. S. Zhao, *ChemSusChem*, 2013, **7**, 2061-2065.
28 V. Papaefthimiou, M. Shishkin, D. K. Niakolas, M. Athanasiou, Y. T. Law, R. Arrigo, D. Teschner, M. Hävecker,; A. Knop-Gericke, R. Schlögl, T. Ziegler, S. G. Neophytides, S. Zafeiratos, *Adv. Energy Mater.*, 2013, **3**, 762-769.
29 S. Mahammadunnisa, P. M. K. Reddy, N. Lingaiah, C. Subrahmanyam, *Catal. Sci. Technol.*, 2013, **3**, 730-736.

30 M. Gong, W. Zhou, M. C. Tsai, J. Zhou, M. Guan, M. C. Lin, B. Zhang, Y. Hu, D. Y. Wang, J. Yang, S. J. Pennycook, B. J. Hwang, H. Dai, *Nat. Commun.*, 2014, **4**, 1-6.

31 Q. Pan, J. Peng, S. Wang, S. Wang, *Catal. Sci. Technol.*, 2014, **4**, 502-509.

32 P. V. R. Rao, V. P. Kumar, G. S. Rao, K. V. R. Chary, *Catal. Sci. Technol.*, 2012, **2**, 1665-1673.

33 W. Zhou, F. Sun, K. Pan, G. Tian, B. Jiang, Z. Ren, C. Tian, H. Fu, *Adv. Funct. Mate*r., 2011, **21**, 1922-1930.

34 S. M. Morris, P. F. Fulvio, M. Jaroniec, *J. Am. Chem. Soc.,* 2008, **130,** 15210-15216.

35 D. Chandra, N. Abe, D. Takama, K. Saito, T. Yui, M. Yaqi, *ChemSusChem*, 2015, **8**, 795-799.

36 X. Du, D. Zhang, L. Shi, R. Gao, J. Zhang, *J. Phys. Chem. C*, 2012, **116**, 10009-10016.

37 T. Odedairo, J. Chen, Z. Zhu, *J. Phys. Chem. C*, 2013, **117**, 21288-21302

38 J. Fan, D. Weng, X. Wu, X. Wu, R. Ran, *J. Catal*., 2008, **258**, 177-186

39 L. Pino, A. Vita, F. Cipitì, M. Laganà, V. Recupero, *Appl. Catal. B: Environ.,* 2011, **104**, 64-73.

40 L. Meng, A. P. Jia, J. Q. Lu, L. F. Luo, W. X. Huang, M. F. Luo, *J. Phys. Chem. C*, 2011, **115**, 19789-19796.

41 Z. Liu, W. Xu, S. Yao, A. C. Johnson-Peck, F. Zhao, P. Michorczyk, A. Kubacka, E. A. Stach, M. Fernández-García, S. D. Senanayake, J. A. Rodriguez, *J. Catal.,* 2015, **321**, 90-99.

42 R. D. Shannon, C. T. Prewitt, *Acta Crystallogr. B*, 1969, **B25**, 925-946.

43 A. Gupta, U. Waghmare, M. Hegde, *Chem. Mater.* 2010, **22**, 5184-5198.

44 J. A. Rodriguez, J. C.Hanson, J. Y. Kim, G. Liu, A. Iglesias-Juez, M. Fernández-García, *J. Phys. Chem. B*, 2003, **107**, 3535-3543.

45 Y. Al-Salik, I. Al-Shankiti, H. Idriss, *J. Electron Spectres.* 2014, **194**, 66-73.

46 R. Grau-Crespo, N. H. de Leeuw, S. Hamad, U.V. Waghmare, *Proc. Royal Soc. A: Math, Phys. Eng. Sci.,* 2011, **467**, 1925-1938

47 L. Barrio, A. Kubacka, G. Zhou, M. Estrella, A. Martínez-Arias, J. C. Hanson, M. Fernández-García, J. A. Rodriguez, *J. Phys. Chem. C*, 2010, **114**, 12689-12697

48 X. Wang, J. A. Rodriguez, J. C. Hanson, D. Gamarra, A. Martínez-Arias, M. Fernández-García, *J. Phys. Chem. B*, 2005, **109**, 19595-19603

49 J. A. Rodriguez, X. Wang, J. C. Hanson, G. Liu, A. Iglesias-Juez, M. Fernández-García, *J. Phys. Chem. B*, 2003, **119**, 5659-5669.

50 P. Zhi-Ying, J. Q. Liu, M. F. Luo, Y. L. Xie, *J. Phys. Chem. C*, 2007, **111**, 18695-18702.

51 M. Guo, J. Lu, Y. Wu, Y. Wang, M. Luo, *Langmuir*, 2011, **27**, 3872-3877.

52 Z. Wu, M. Li, J. Howe, H. M. Meyer, S. H. Overbury, *Langmuir*, 2010, **26**, 16595-16606.

53 L. Li, F. Chen, J. Q. Lu, M. F. Luo, *J. Phys. Chem. A*, 2011, **115**, 7972-7977

54 R. Gao, D. Zhang, P. Maitarad, L. Shi, T. Rungrotmongkol, H. Li, J. Zhang, W. Cao, *J. Phys. Chem. C*, 2013, **117**, 10502-10511

55 S. L. Zhong, L. F. Zhang, L. Wang, W. X. Huang, C. M. Fan, , A. W. Xu, *J. Phys. Chem. C*, 2012, **116**, 13127-13132

56 D. H.,Prasad, S. Y. Park, H. I. Ji, H. R. Kim, J. W. Son, B. K. Kim, H .W. Lee, J. H. Lee, *J. Phys. Chem. C*, 2012, **116**, 3467-3476

57 W. Y. Herna´ndez, M. A. Centeno, F. Romero-Sarria, J. A. Odriozola, *J. Phys. Chem. C*, 2009, **113**, 5629-5635

58 V. J. Ferreira, P. Tavares, J. L. Figueiredo, J. L. Faria, *Ind. Eng. Chem. Res.,* 2012, **51**, 10535-10541

59 P. V. R. Rao, V. P. Kumar, G. S. Rao, K.V. R. Chary, *Catal. Sci. Technol.*, 2012, **2**, 1665-1673.

60 R. Pérez-Hernández, G. Mondragón-Galicia, A. A. Maravilla, J. Palacios, *Phys. Chem. Chem. Phys.*, 2013, **15**, 12702-12708.

61 L. Wang, H. Liu, Y. Liu, Y. Chen, S. J. Yang, *Rare Earth*, 2013, **31**, 559-564

62 L. Jalowiecki-Duhamel, C. Pirez, M. Capron, F. Dumeignil, E. Payen, *Inter. J. Hydrogen Energy*, 2010, **35**, 12741-12750.

63 G. Zhou, L. Barrio, S. Agnoli, S. D. Senanayake, J. Evans, A. Kubacka, M. l. Estrella, J. C. Hanson, A. Martnez-Arias, F. G. Marcos, J. Rodriguez, *Angew. Chem. Inter. Ed.*, 2010, **49**, 1-6.

64 J. Z. Luo, Z. L. Yu, C. F. Ng, C. T. Au, *J. Catal.*, 2000, **194**, 198-210.

65 X. Chen, J. Jiang, S. Tian, K. Li, *Catal. Sci. Technol.*, 2015, **5**, 860-868.

66 D. Liu, X. Y. Quek, W. N. E. Cheo, R. Lau, A. Borgna, Y. Yang, *J. Catal.,* 2009, **266**, 380-390

67 L. Mo, K. K. M. Leong, S. Kawi, *Catal. Sci. Technol.*, 2014, **4**, 2107-2114.

68 N. Wang, Z. X. Xu, J. Deng, K. Shen, X. Yu, W. Qian, W. Chu, F. Wei, *ChemCatChem*, 2014, **6**, 1470-1480.

69 Z. X. Xu, N. Wang, W. Chu, J. Deng, S. Luo, *Catal. Sci. Technol.*, 2015, **5**, 1588, 1597.

70 M. A. Ebiad, D. R. Abd El-Hafiz, R. A. Elsalamony, L. S. Mohamed, *RSC Adv.*, 2012, **2**, 8145-8156.

71 Y. Yang, W. Li, H. Xu, *React. Kinet. Catal. Lett.*, 2002, **77**, 155-162.

72 F. Cova, D. G. Pintos, A. Juan, B. rigoyen, *J. Phys. Chem. C*, 2011, **115**, 7456-7465.

73 P. Kratzer, B. Hammer, J. K. Nørskov, *J. Chem. Phys.*, 1996, **105**, 5595-5604.

74 N. Sun, X. Wen, F. Wang, W. Peng, N. Zhao, F. Xiao, W. Wei, Y. Sun, J. Kang, *Appl. Surf. Sci.*, 2011, **257**, 9169-9176.

75 S. Q. Chen, Y. Liu, *Inter. J. Hydrogen Energy*, 2009, **34**, 4735-4746.

76 Z. Li, X. Hu, L. Zhang, S. Liu, G. Lu, *Appl. Catal. A: Gen.*, 2012, **417-418**, 281-289.

77 D. Baudouin, U. Rodemerck, F. Krumeich, A. de Mallmann, K. C. Szeto, H. Ménard, L. Veyre, J. P. Candy, P. B. Webb, C. Thieuleux, C. Copéret, *J. Catal.*, 2013, **297**, 27-34.

78 Q. Liang, L. Z. Gao, Q. Li, S. H. Tang, B. C. Liu, Z. L. Yu, *Carbon* 2001, **39**, 897-903

TOC Graphics

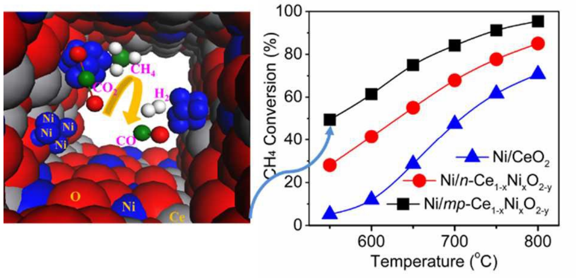

A heterostructure of highly dispersed Ni nanoparticles in pore channels of Ni-CeO_2 solid solution, having the excellent thermo-stability, redox property, and metal/support synergy, is identified as an efficient nanocatalyst for converting greenhouse house into H_2 energy and syngas